Dalton Transactions

PAPER

View Article Online
View Journal | View Issue

Cite this: *Dalton Trans.*, 2026, **55**, 5667

Structural characterization, proton conductivity and furfural catalysis of novel polyfunctional zirconium phosphonates

Montse Bazaga-García,[a,b] Rosario M. P. Colodrero,[a,c] Álvaro Vílchez-Cózar,[a,c] Pascual Olivera-Pastor,[a,c] Juan A. Cecilia,[a,d] Łukasz Kurowski,[e] Jan K. Zaręba *[e] and Aurelio Cabeza *[a,c]

Zirconium phosphonates combine the thermal robustness of Zr–O frameworks with the rich functionality of organophosphonic linkers, making them attractive for both energy-related and catalytic applications. Here, we report three new crystalline Zr(IV) phosphonates built from 5-(dihydroxyphosphoryl)-isophthalic acid (**PiPhtA**), 5-(dihydroxyphosphoryl)-nicotinic acid (**PNA**) and benzene-1,2,3-triyltris(methylenephosphonic acid) (**BTTMPA**). Phase-pure $Zr[(HO_3P\text{-}C_6H_3\text{-}(COOH)_2)_2(X)_2]\cdot 6H_2O$ (X = F^-/OH^-) (**Zr-PiPhtA**), $Zr(O_3P\text{-}NH^+\text{-}C_5H_3\text{-}COOH)_2F_2$ (**Zr-PNA**) and $Zr[(H_2O_3PCH_2)(O_3PCH_2)_2\text{-}C_6H_3]\cdot H_2O$ (**Zr-BTTMP**) were obtained under mild solvothermal conditions and characterized by synchrotron powder X-ray diffraction, pair distribution function (PDF) analysis, solid-state NMR and thermogravimetry. The crystal structures of 1D **Zr-PNA** ($P2_1/c$) and 3D **Zr-BTTMP** ($P2_1/a$) were solved *ab initio* from powder diffraction data, while combined structural X-ray diffraction and PDF analyses together with ammonia adsorption suggest that nanocrystalline **Zr-PiPhtA** exhibits features resembling those of the analogous **Ca-PiPhtA** derivative and **Zr-BTTMP**. Given that all of them exhibit characteristics adequate for facilitating proton transfer pathways, a study of proton conductivity was undertaken. Under 95% relative humidity, bulk proton conductivities reach 1.2×10^{-3} S cm^{-1} (**Zr-BTTMP**) at 80 °C. On exposure to NH_3 vapour, the conductivity of **Zr-PiPhtA** and **Zr-PNA** increased by almost one order of magnitude, up to 3.2×10^{-3} S cm^{-1} at 80 °C for **Zr-PiPhtA**, highlighting the decisive role of ammonium-assisted proton hopping. The same acid sites that promote proton mobility also endow the materials with bifunctional catalytic behavior. In the one-pot cascade upgrading of furfural, **Zr-PiPhtA** afforded the highest overall conversions, benefiting from the nanocrystalline morphology and a higher density of strong Brønsted acid sites.

Received 9th December 2025,
Accepted 10th March 2026

DOI: 10.1039/d5dt02947c

rsc.li/dalton

Introduction

Zr-based multifunctional phosphonates constitute a sub-type of coordination polymers[1] distinguished by their remarkable chemical and thermal stability. Such properties make them attractive for applications in catalysis,[2,3] ion exchange/intercalation,[4–9] antibacterial treatments,[10,11] proton conductivity,[12–16] *etc*. In particular, the open framework, Zr(IV) polyphosphonate $[Zr_2(H_4TPPP)(OH/F)_2]\cdot xH_2O$ ($H_{10}TPPP$ = 5,10,15,20-(tetra-4-phosphonatophenyl)porphyrin), has been demonstrated to exhibit high proton conductivity (1.2×10^{-3} S cm^{-1}, 95% RH, 298 K) besides light-harvesting properties in the UV-visible–NIR regions.[17] In addition, specific functionalization can be implemented by appropriate attachment of organic moieties, like carboxylic or amino groups, to the backbone of the phosphonic ligand.[18] Thus, materials with enhanced proton conductivity have been reported.[19–21] Furthermore, post-synthetic modification through the incorporation of guest molecules, such as ($Me_2NH_2^+$) or ammonium (NH_4^+), is possible, giving rise to the formation of extended hydrogen bond networks and, therefore, increased proton conductivity.[22–30]

Zirconium phosphates and phosphonates have been extensively employed as acid catalysts in processes, including the conversion of furfural (FUR)[31] into interesting products such as polymers, fuels, additives, and solvents, among others.[32] Zirconium phosphate/phosphonate-based catalysts contain

[a]*Departamento de Química Inorgánica, Cristalografía y Mineralogía, Facultad de Ciencias, Universidad de Málaga, Campus Teatinos s/n, 29071-Málaga, Spain. E-mail: aurelio@uma.es*
[b]*Departamento de Química Inorgánica, Universidad de Salamanca, Plaza de los Caídos s/n, 37008 Salamanca, Spain*
[c]*Instituto Universitario de Materiales y Nanotecnología, IMANA, Universidad de Málaga, Campus Teatinos s/n, 29071-Málaga, Spain*
[d]*Instituto de Investigación de Biorrefinerías "I3B", Facultad de Ciencias, Universidad de Málaga, Campus Teatinos s/n, 29071-Málaga, Spain*
[e]*Institute of Advanced Materials, Faculty of Chemistry, Wrocław University of Science and Technology, 50-370 Wrocław, Poland. E-mail: jan.zareba@pwr.edu.pl*

Lewis-acidic zirconium centers and Lewis-basic phosphate/phosphonate groups, which play a significant role in enhancing their catalytic performance as demonstrated for the conversion of furfural, levulinic acid (LA) and LA esters to produce valuable molecules under mild reaction conditions.[33,34]

In this work, we report the synthesis, crystal structures, proton conductivity and catalytic behaviour of three new zirconium(IV) phosphonates derived from multifunctional phosphonic acids: 5-(dihydroxyphosphoryl)-isophthalic acid (**PiPhtA**), 5-(dihydroxyphosphoryl)-nicotinic acid (**PNA**) and benzene-1,2,3-triyltris(methylenephosphonic acid) (**BTTMPA**), the latter described here for the first time. By combining **PiPhtA** with metal ions such as Cu^{2+},[35] Ca^{2+},[35] and lanthanide ions,[23–25,35] a diverse set of frameworks (2D and 3D) were obtained. Some of them, specifically ammonia-adsorbed calcium,[24] and some lanthanide derivatives $Yb[O_3P\text{-}C_6H_3(COO)(COOH)(H_2O)]$,[33] exhibited proton conductivities of up to 5×10^{-3} S cm^{-1} at 80 °C and 95% RH. On the other hand, metal **PNA** derivatives have been studied only as luminescent (Zn^{2+}–, Cd^{2+}–, and Co^{2+}) or magnetic (Co^{2+}– and Ni^{2+}–) materials.[36–38] Herein, we investigate zirconium(IV) derivatives of these multifunctional phosphonic acids as both proton conductors and catalysts toward FUR conversion, aiming to determine the structures/properties of these acidic materials.

Experimental

Materials and general characterization

All chemicals used in the synthesis were readily available from commercial sources (Merck or VWR) and used as received. Elemental analyses (C, H, and N) were carried out using a PerkinElmer 240 analyser. Zr and P contents were determined by ICP-MS using a PerkinElmer Nexion 300D analyser. Thermogravimetric analyses (TGA) were performed using an SDT-Q600 analyser in open platinum crucibles under an air flow at a heating rate of 10 °C min^{-1}. ATR FT-IR spectra were recorded using a Jasco FTIR 6800FV spectrometer equipped with an ATR Pro One accessory without treatment of samples. All spectra were recorded in the 4000–400 cm^{-1} range at 4 cm^{-1} resolution, and 64 scans were accumulated. ^{1}H and ^{31}P (^{1}H-decoupled) spectra in solution were recorded using Jeol JNM-ECZ400SL1 or Bruker Avance III 600 instruments at the indicated frequencies and are referred to as a residual solvent signal. ^{31}P MAS-NMR spectra were recorded at RT with an AVANCE III HD 600 (Bruker AXS) spectrometer using a triple-resonance CP-MAS probe of 3.2 mm at a spinning rate of 15 kHz and a contact time of 3 ms. XPS spectra were recorded using a Physical Electronics ESCA5701 spectrometer.

Synthesis

Synthesis of phosphonic acids. The **PiPhtA** and **PNA** ligands were prepared following the methods reported by Bazaga-García M. *et al.*[24] and Zoń *et al.*,[39] respectively, and their structures are shown in Scheme 1.

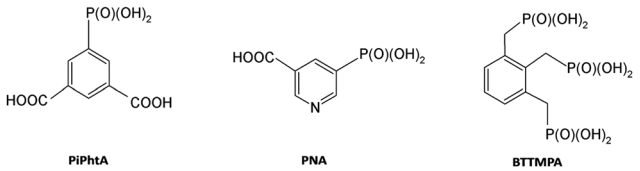

Scheme 1 Structure of ligands **PiPhtA**, **PNA** and **BTTMPA**.

Benzene-1,2,3-triyltris(methylenephosphonic acid) (**BTTMPA**) was prepared from 1,2,3-trimethylbenzene according to the synthetic route shown in Scheme 2.

*1,2,3-tris(bromomethyl)benzene (**1**).* A mixture of 1,2,3-trimethylbenzene (also known as hemellitol, 10 mL, 74.4 mmol, 90% purity), *N*-bromosuccinimide (43.69 g, 245 mmol, 3.3 equivalents), and dibenzoyl peroxide (0.050 g) in chloroform (150 mL) was refluxed for 3 hours. After cooling to room temperature, the succinimide precipitate was removed by suction filtration. The filtrate was then evaporated under reduced pressure, yielding a crude light-orange product. This product was recrystallized twice from acetone to afford a white crystalline product (9.265 g, 35%). ^{1}H NMR (400 MHz, $CDCl_3$, 300 K) δ 7.38–7.22 (m, 3H), 4.81 (s, 2H), 4.60 (s, 4H) ppm. The obtained spectral data are consistent with previously reported literature values.[40,41]

*Hexaethyl benzene-1,2,3-triyltris(methylenephosphonate) (**2**).* The phosphonylation of 1,2,3-tris(bromomethyl)benzene (**1**) was achieved using the Arbuzov reaction. Specifically, 1,2,3-tris(bromomethyl)benzene (3.00 g, 8.41 mmol) and triethyl phosphite (15 mL, 87.4 mmol) were placed in a two-necked 50 mL flask equipped with a gas inlet, a volatiles trap, and a stirring bar. The flask was immersed in a silicone oil bath and heated to 150 °C while nitrogen gas was passed vigorously through the reaction system to effectively remove ethyl bromide, a by-product of the reaction. The reaction mixture was stirred under these conditions for 2 hours. After cooling to room temperature, hexane (50 mL) was added to induce phase separation. The resulting milky mixture was placed in a freezer at −18 °C for approximately 1 hour, resulting in the separation of a sticky light brown oil. The hexane layer, containing excess triethyl phosphite, was decanted, and the procedure was repeated. The crude product was purified using column chromatography on silica gel (pore size 60 Å, 40–63 μm) with a solvent system consisting of ethyl acetate, ethanol, and acetic acid in a 100 : 10 : 1 v/v ratio. The product was visualized using silica gel plates with a fluorescent indicator (254 nm) and a UV lamp, showing an R_f value of 0.25. Compound (**2**) was obtained in a yield of 41% (1.801 g) as a light brown viscous oil. ^{1}H

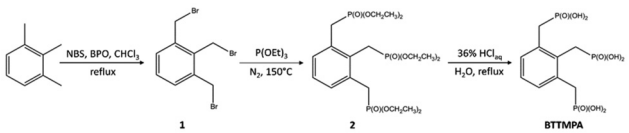

Scheme 2 Synthetic route to **BTTMPA**.

NMR (400 MHz, $CDCl_3$, 300 K) δ 7.23–7.05 (m, 3H), 4.10–3.82 (m, 12H), 3.67 (d, $^2J_{H-P}$ = 20.9 Hz, 2H), 3.49–3.26 (br d, 4H), 1.225 (t, 6H, $^3J_{H-H}$ = 7.1 Hz), 1.22 (t, 12H, $^3J_{H-H}$ = 7.1 Hz) ppm. $^{31}P\{^1H\}$ NMR (162 MHz, $CDCl_3$, 300 K) δ 27.85 (t, J_{P-P} = 9.5 Hz, 1P), 27.27 (d, J_{P-P} = 9.5 Hz, 2P) ppm.

*Benzene-1,2,3-triyltris(methylenephosphonic acid) (**BTTMPA**).* Compound (**2**) (1.006 g, 1.9 mmol), deionized water (20 mL), and hydrochloric acid solution (36% aqueous, 20 mL) were placed in a flask and refluxed for 16 hours. The resulting light brown solution was filtered, and the filtrate was evaporated under reduced pressure to yield a light brown solid. This solid was then dissolved in methanol (50 mL). Activated carbon (approximately 100 mg) was added to the solution, and the suspension was briefly refluxed. The mixture was filtered through Celite and evaporated to dryness, yielding **BTTMPA** as a beige solid (0.509 g, 74%). ^1H NMR (600 MHz, D_2O, 300 K) δ 7.08 (d, $^3J_{H-H}$ = 7.4 Hz, 2H), 6.96 (t, $^3J_{H-H}$ = 7.5 Hz, 1H), 3.22 (d, J = 19.4 Hz, 2H), 3.01 (d, J = 19.2 Hz, 4H) ppm. $^{31}P\{^1H\}$ NMR (243 MHz, D_2O, 300 K) δ 19.47 (s, 2P), 19.37 (s, 1P) ppm.

Synthesis of $Zr[(HO_3P\text{-}C_6H_3\text{-}(COOH)_2)_2(X)_2]\cdot 6H_2O$ ($X = F^-/OH^-$) (Zr-PiPhtA). 0.488 g (2 mmol) of the ligand 5-(dihydroxyphosphoryl)-isophthalic acid (**PiPhtA**) was solubilized in 40 mL of deionized water. A total of 0.324 g (1 mmol) of zirconium oxychloride octahydrate was dissolved in 5.17 mL of 2.9 M hydrofluoric acid solution (HF/Zr^{4+} molar ratio = 15/1). These two solutions were mixed in a closed plastic bottle, and the reaction mixture was heated to 80 °C for 8 days and then cooled to room temperature. The solid was filtered under vacuum, washed several times with deionized water, and air-dried for 24 h. Elemental analysis: calculated (%): C 26.44, H 3.33; found (%): C 26.11, H 3.35. Yield: 75.1%, based on zirconium.

Synthesis of $Zr(O_3P\text{-}NH^+\text{-}C_5H_3\text{-}COOH)_2F_2$ (Zr-PNA). A total of 0.04062 g (0.2 mmol) of the ligand 5-(dihydroxyphosphoryl) nicotinic acid (**PNA**) was solubilized in 1.3 mL of deionized water. A total of 0.0645 g (0.2 mmol) of $ZrOCl_2\cdot 8H_2O$ was dissolved in 0.69 mL of 2.9 M HF solution (HF/Zr^{4+} molar ratio = 10/1). These two solutions were mixed in a closed plastic bottle. Next, the reaction mixture was transferred to a Teflon-lined reactor and heated at 150 °C for 2 days and then cooled down to room temperature. The solid was filtered under vacuum, washed several times with deionized water and once with ethanol, and air-dried for 24 h. Elemental analysis: calculated (%): C: 26.92, H: 2.26, N: 5.23; found (%): C: 26.72, H: 2.26; N: 4.95. Yield: 53.6%, based on zirconium.

Synthesis of $Zr[(H_2O_3PCH_2)(O_3PCH_2)_2\text{-}C_6H_3]\cdot H_2O$ (Zr-BTTMP). 0.0720 g (0.2 mmol) of **BTTMPA** was solubilized in 1 mL of deionized water. A total of 0.0645 g (0.2 mmol) of $ZrOCl_2\cdot 8H_2O$ was dissolved in 0.69 mL of 2.9 M HF solution (HF/Zr^{4+} molar ratio = 10/1). Both solutions were mixed in a closed plastic bottle and, afterwards, the reaction mixture was transferred to a Teflon-lined reactor and heated at 150 °C for 2 days. After cooling to room temperature, the resulting solid was filtered and washed as previously described. Elemental analysis: calculated (%): C 23.23, H 2.82; found (%): C 23.36, H 2.74. Yield: 64.3%, based on zirconium.

NH_3 and pyridine adsorption

The ammonia-adsorbed derivatives were prepared according to a previously reported procedure.[24] 100 mg of the as-synthesized solids were placed in contact with ammonia vapours from a 2 M solution of NH_3 in a closed container for several hours until a constant composition was achieved (<24 h). Elemental analysis of NH_3-loaded Zr-phosphonates: $Zr[(HO_3P\text{-}C_6H_3\text{-}(COOH)_2)_2X_2](H_2O)_6(NH_3)_{6.5}$ ($X = F^-/OH^-$) (**Zr-PiPhtA_NH$_3$**), calc.: C 22.98%; H 5.00%; N 10.89%. Found: C 22.96%; H 4.76%; N 10.8%; $Zr[(O_3P\text{-}NH^+\text{-}C_5H_3\text{-}COOH)_2F_2](H_2O)_{4.5}(NH_3)_6$ (**Zr-PNA_NH$_3$**), calc.: C 21.30%; H 4.5%; N 10.49%. Found: C, 20.81%; H, 3.71%; N, 10.54%.

The adsorption of pyridine was evaluated by suspending 30 mg of each material in 1 mL of pyridine and stirred for 30 min. The solids were then isolated by centrifugation, washed three times with acetone and dried at 60 °C overnight. The amount of pyridine adsorbed was determined by elemental analysis.

Structure determination

Routine laboratory X-ray powder diffraction (LXRPD) patterns were obtained using an Empyrean PANalytical diffractometer (Cu $K\alpha_{1,2}$) equipped with a PIXcel 1D detector in a Bragg–Brentano configuration between 4° and 70° (2θ), a step size of 0.013° and a counting time of ~24 s per step. For the structural determination of **Zr-PNA** and **Zr-BTTMP**, LXRPD patterns were recorded in a capillary of 0.5 mm diameter using a D8 ADVANCE (Bruker AXS) diffractometer equipped with a Johansson Ge (111) primary monochromator, giving monochromatic Mo radiation, and an EIGER detector. The samples were measured between 1.6 and 49.9° (2θ), with a 0.0167° step size and a total measurement time of approximately 5 hours. Crystal structures of **Zr-PNA** and **Zr-BTTMP** were solved using the EXPO2014 program[42] and optimized by the Rietveld method[43] using the GSASII program.[44] Soft constraints were imposed to preserve chemically reasonable geometries for phosphonate and carboxylic groups and the aromatic ring. The Rietveld plots are shown in Fig. S1 and S2 for **Zr-PNA** and **Zr-BTTMP**, respectively. All crystallographic data are given in Table 1. For studying the dehydration-rehydration processes in **Zr-PiPhtA** and **Zr-BTTMP**, thermodiffractometric studies were carried out using a PANalytical X'Pert Pro diffractometer in an Anton Paar TTK450 camera using $CuK_{\alpha 1}$ radiation and an X'Celerator detector. For **Zr-PiPhtA**, the data were collected at different temperatures between 30 °C and 140 °C, under static air. For **Zr-BTTMP**, the data were obtained under an N_2 flow in the range of 30–350 °C.

For PDF analysis of **Zr-PiPhtA**, the synchrotron XRPD (SXRPD) data were obtained at the BL04-MSPD beamline of the ALBA Synchrotron (Spain) using a wavelength of 0.3257(1) Å (38 keV). The final dataset was obtained by merging four patterns, each one measured for 38 min from 1° to 130° (2θ). The experimental PDF data were obtained using PDFgetX3 software,[45] using a Q_{max} value of 18 $Å^{-1}$. Nickel was used as a standard for the determination of the instrumental parameters

Table 1 Crystallographic data for **Zr-PNA** and **Zr-BTTMP** compounds

Compound	**Zr-PNA**	**Zr-BTTMP**
Chemical formula	$ZrC_{12}H_{12}N_2F_2O_{10}P_2$	$ZrC_9H_{14}O_{10}P_3$
Weight (M_r, g mol^{-1})	535.39	466.34
Crystal system	Monoclinic	Monoclinic
Space group	$P2_1/c$	$P2_1/a$
λ (Å)	0.7093	0.7093
a (Å)	5.24914(16)	14.9748(19)
b (Å)	14.8202(5)	17.2635(10)
c (Å)	10.6344(4)	5.2988(4)
β (°)	90.9414(19)	95.481(5)
Volume (Å^3)	827.18(5)	1363.57(16)
Z	2	4
ρ_{calc} (g cm^{-3})	2.1010	2.2029
2θ range (°)	1.32–49.99	2.0–44.0
No. of independent reflections	1459	2150
Data/restraints/parameters	2915/32/71	1683/63/99
R_{wp}	0.05479	0.02877
R_p	0.03761	0.02246
R_F	0.02701	0.02990
CCDC	2303570	2303569

Q_{damp} (0.003706 Å^{-1}) and Q_{broad} (0.0123706 Å^{-1}). PDFgui software[46] was used for the analysis/simulation of PDF data.

Catalysis tests

The tests were performed in glass pressure reactors with thread bushing (acetic acid, 15 mL). For each test, 25 mg of the sample was mixed with 0.1 mmol of FUR and 2-propanol (4 mL), maintaining a 2-propanol/FUR molar ratio of 50 : 1. In a preliminary step, the reactors were purged with a N_2 flow. Reactions were performed in an aluminium block, where the temperature was controlled with a thermocouple immersed in the block, under continuous stirring (400 rpm), and different reaction times at 170 °C. After the reaction, glass reactors were withdrawn from the aluminium block and immersed in water, cooling down the reaction mixture to room temperature. Then, a portion of the reaction medium was microfiltered to take an aliquot, which was analyzed by gas chromatography using a flame ionization detector and a CP-Wax 52 CB capillary column. The FUR conversion and yield were calculated as follows:

$$\text{Conversion (\%)} = (\text{mol of furfural converted/mol of furfural fed}) \times 100$$

$$\text{Yield (\%)} = (\text{mol of product/mol of furfural fed}) \times 100$$

For comparative catalytic studies, zirconium phosphate was synthesized following the previously reported procedure.[47]

Proton conductivity measurements

Impedance data were recorded on cylindrical pellets (diameter ~ 5.03–5.09 mm and thickness ~ 1–1.20 mm) obtained by pressing ~35–40 mg of the sample at 2 MPa for 2 min, which were pressed between porous C electrodes (Sigracet, GDL 10 BB, no Pt). The sample cell was placed inside a temperature- and humidity-controlled chamber (Espec SH-222). The AC impedance data were collected using an AUTOLAB PGSTAT302N equipped with a frequency response analyser (FRA 32M) over the frequency range from 0.1 Hz to 1 MHz at an applied voltage between 0.15 and 0.35 V. To equilibrate water content, the pellets were preheated (0.2 °C min^{-1}) from 40 to 80 °C under relative humidities (RH) of 95 and 75%. Impedance spectra were recorded during cooling and the samples were equilibrated at each temperature using an initial stabilization time of 8–10 hours, except for **Zr-PNA_NH$_3$**, which required at least 24 h. Water condensation on the sample was avoided by reducing relative humidity before decreasing temperature. The calculated densities for **Zr-BTTMP** (1.531 g cm^{-3}) and **Zr-PNA** (1.727 g cm^{-3}) correspond to compaction degrees of 72.1 and 82.2%, respectively. For **Zr-PiPhtA**, the experimental density was 1.53 g cm^{-3}. For the ammonia-loaded samples, the experimental densities were 1.50 and 1.63 g cm^{-3} for **Zr-PiPhtA_NH$_3$** and **Zr-PNA_NH$_3$**, respectively.

Results and discussion

Chemical and structural characterization

Elemental analysis (C, N, and H), TG, ICP (Zr and P) and XPS (Zr/F and Zr/P molar ratios, Fig. S3) were used to determine the chemical composition of the different solids. Due to the use of HF in the synthesis, derivatives of **PiPhtA** and **PNA** ligands are fluorinated compounds. In addition, for **Zr-PNA**, the N1s XPS signal at 401.1 eV supports the presence of quaternary N^+–H species (Fig. S3).[48]

The anhydrous fluorinated solid **Zr-PNA**, $Zr(O_3P\text{-}NH^+\text{-}C_5H_3\text{-}COOH)_2F_2$, crystallizes in the monoclinic system with the space group $P2_1/c$ and its crystal structure was solved *ab initio* using LXRPD (Table 1). The asymmetric unit contains one zirconium atom situated in the special position, one 5-(dihydroxyphosphoryl) nicotinate ligand and one F^- ion (Fig. 1a). Four equatorial oxygens from four phosphonate ligands and two axial F^- ions compose the octahedral environment of each Zr^{4+} ion (Fig. 1a). The phosphonate groups bridge adjacent Zr^{4+} ions and form the chains of isolated zirconium octahedra, running along the *a*-axis (Fig. 1b). The chains are further interconnected through H-bonds between the protonated carboxylate groups and the oxygen from the phosphonate group [$d_{(O4\cdots O2)}$ = 2.53(2) Å], as well as between the N^+–H groups and the F^- ions [$d_{(N-H\cdots F)}$ = 2.73(2) Å] (Fig. 1c).

The ^{31}P MAS-NMR spectrum of this compound (Fig. 2) exhibits only one signal centred at −6.8 ppm, which accords with the presence of a crystallographically independent deprotonated phosphonate group. On the other hand, the FTIR spectra (Fig. S4) are consistent with the presence of uncoordinated carboxylic groups, displaying vibration bands at 1703 and 1603 cm^{-1}, corresponding to the antisymmetric $\nu_{C=O}$ vibrations, and at 1449 and 1402 cm^{-1}, assigned to the symmetric ν_{C-O} stretching.

Thermal analysis of **Zr-PNA** (Fig. S5) shows a continuous weight loss between 350 and 700 °C, attributable to an over-

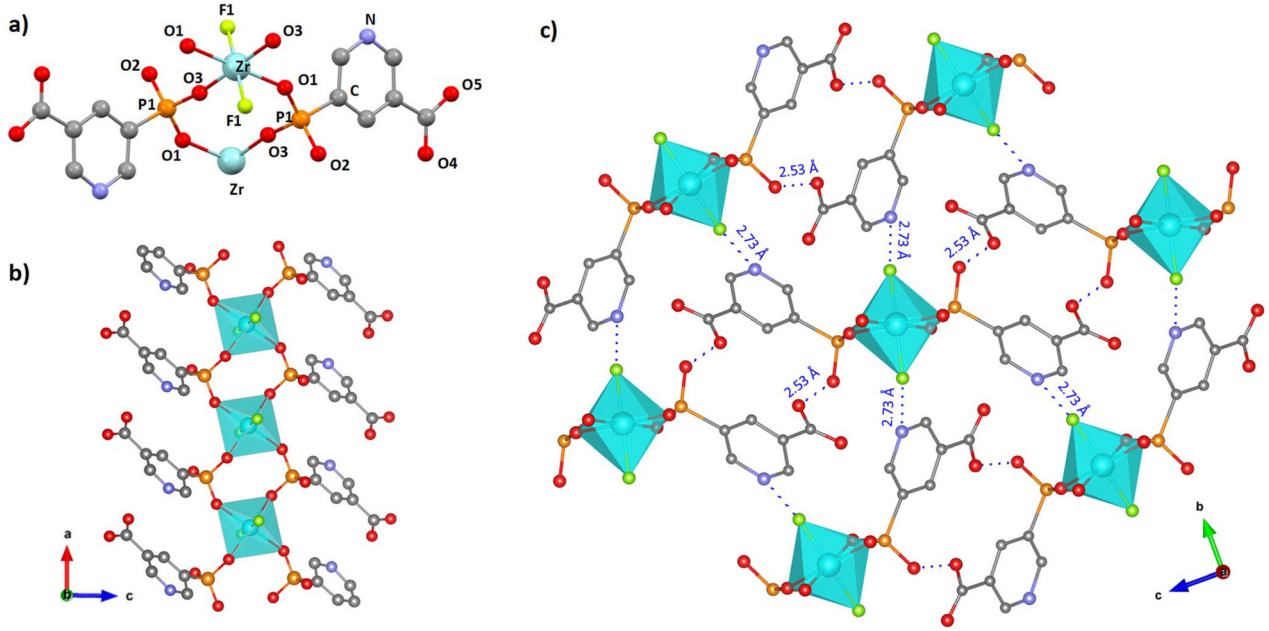

Fig. 1 Crystal structure details of **Zr-PNA**: (a) extended view of the asymmetric unit showing the octahedral coordination environment of Zr^{4+} and the connectivity of the ligand. (b) A view of the chains along the *b*-axis. (c) Packing of chains in the *bc* plane. Colours: Zr (cyan), P (orange), F (light green), N (light blue), O (red) and C (grey).

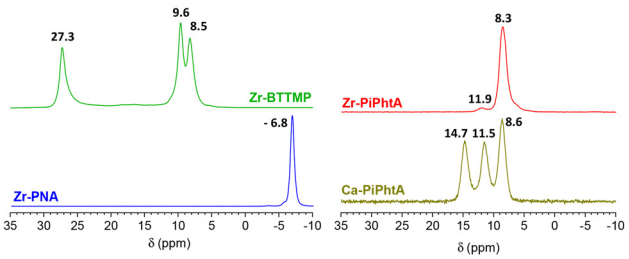

Fig. 2 ^{31}P MAS-NMR spectra of the Zr^{4+} and Ca^{2+} derivatives.

lapped removal of HF and decomposition of the phosphonate ligand, leading to the formation of ZrP_2O_7 (PDF 01-085-0896), according to the LXRPD data. FTIR analysis of **Zr-BTTMP**, $Zr[(H_2O_3PCH_2)(O_3PCH_2)_2\text{-}C_6H_3]\cdot H_2O$, suggests the presence of water in this compound (Fig. S4), which agrees well with one water molecule per formula unit (calc. 3.87% and obs. 3.26%), as demonstrated by elemental and thermal analyses (Fig. S5). According to the TG curve, the sustained weight loss between 150 °C and about 500 °C corresponds to the removal of water, while the decomposition of the ligand takes place between 500 and 900 °C.

Zr-BTTMP crystallizes in the monoclinic system with space group $P2_1/a$ (Table 1). The asymmetric unit consists of one Zr^{4+} ion and one ligand molecule (Fig. 3a). The phosphonate groups bridge Zr^{4+} ions through O4 and O6 (P2) and O7, O8 and O9 (P3), forming two-fold arrays of interconnected ZrO_6 polyhedra parallel to the *c*-axis (Fig. 3b). The octahedral environment around the zirconium ion is completed with another oxygen (O2) from P1. The oxygen atoms O1 and O3, from P1, and O5, from P2, remain uncoordinated and point toward the cavities, facilitating hydrogen-bond interaction pathways along the *c*-axis (Fig. 3c). According to this structural arrangement, the ^{31}P MAS-NMR signal at 27.3 ppm (Fig. 2) can be assigned to P1, which exhibits the lowest connectivity to Zr^{4+}, while the upfield bands, at 9.6 and 8.3 ppm, correspond to P2 and P3, bridging two and three Zr^{4+} ions, respectively.

Although **Zr-BTTMP** is a monohydrate compound, the presence of internal water could not be located from the LXRPD data. Thus, we carried out thermodiffraction and Rietveld refinement studies to further investigate the location of this water. Upon heating up to 350 °C and further cooling to RT under N_2, no structural changes could be observed from the Rietveld refinement (see Table S1), which remained practically unmodified on cooling under dried conditions, pointing to the absence of structural water that otherwise some lattice distortion could be detected. Moreover, the compound reversibly rehydrated upon cooling to RT in air (Fig. S6). Consequently, we attribute the hydration of this compound to strongly adsorbed water on the particle surface.

The SXRPD pattern of **Zr-PiPhtA** was indexed using the DICVOL program[49] in a monoclinic unit cell with parameters a = 13.909(8) Å, b = 5.590(1) Å, c = 13.793(3) Å, β = 106.26(4)° and V = 1029 (1) Å^3 [$M(20)$ = 12.6; $F(20)$ = 108.6(0.0033, 55)]. However, the low crystallinity of this compound did not allow solving its crystal structure. The TG curve corresponding to **Zr-PiPhtA** (Fig. S5) displays a first weight loss between 80 and 130 °C corresponding to the removal of all lattice water molecules (weight loss found: 15.26%; calculated: 15.94%).

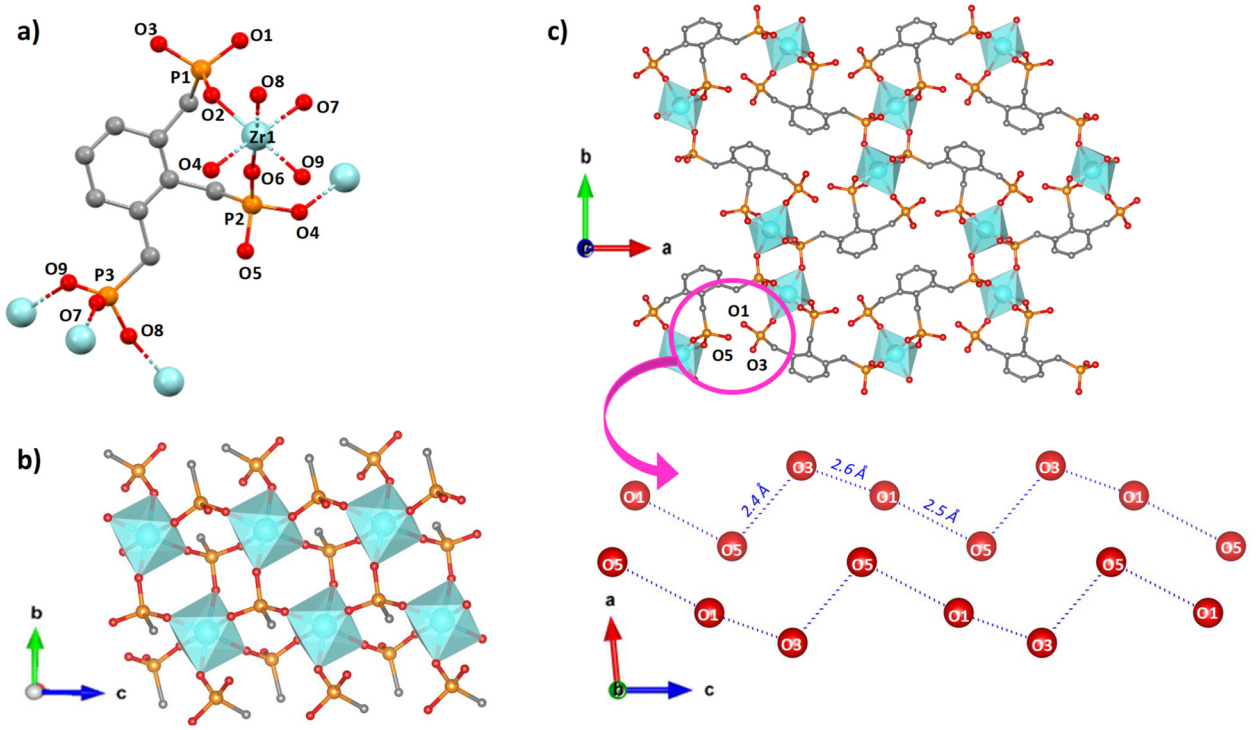

Fig. 3 Crystal structure details of **Zr-BTTMP**: (a) extended asymmetric unit showing the connectivity of the BTTMP ligand to the Zr^{4+} ion. (b) Zirconium octahedral two folded chains viewed along the *c*-axis. (c) 3D structure and H-bond pathways along the *c*-axis.

After dehydration, the solid decomposes in two steps. The first one, 300–350 °C, correlates with the removal of HF and dehydroxylation with an associated weight loss of 6.0% (calculated: 5.4%). The second step, associated with an exothermic peak in the DTA curve, corresponds to the combustion of the organic matter, leading to the formation of ZrP_2O_7 (PDF 01-085-0896) at 900 °C, as identified by LXRPD. The thermodiffractometric analysis of **Zr-PiPhtA** (Fig. S6) reveals that this solid dehydrates completely at 140 °C, resulting in a poorly crystalline solid. Upon water removal, a shift of the first diffraction peak at higher 2θ values as compared with the hydrated phase indicates a shrinkage of the structure, which experiences a reversible rehydration in air. A similar behaviour was observed for the pillared-layered compound $Ca_2[HO_3PC_6H_3(COOH)_2]_2[(HO_3PC_6H_3(COO)_2H)(H_2O)_2]\cdot 5H_2O$ (**Ca-PiPhtA**).[24] The FTIR spectrum of this compound (Fig. S4) reveals the presence of the carboxylic group in the ligand, with characteristic antisymmetric $\nu_{C=O}$ and symmetric ν_{C-O} vibration modes as observed for **Zr-PNA**, as well as those corresponding to the aromatic rings, phosphonate groups and lattice water. The ^{31}P MAS-NMR spectrum of **Zr-PiPhtA** (Fig. 2) displays a main signal with an isotropic chemical shift at 8.3 ppm and a weak peak at 11.9 ppm. Although with different relative intensities, these δ_{iso} positions are quite similar to those observed for **Ca-PiPhtA**,[24] (Fig. 2). The signals at 8.6 and 11.5 ppm in the ^{31}P MAS-NMR spectrum of **Ca-PiPhtA** are attributed to the monoprotonated phosphonate groups connected to three metal ions in a bridging plus chelate fashion, but with different H-bond interactions with the lattice water molecules. The absence of a downfield signal in the ^{31}P MAS-NMR spectrum of **Zr-PiPhtA**, as compared with that of the calcium derivative, which displays a third peak at 14.7 ppm, suggests that a higher metal–dicarboxyphosphonate ligand connectivity exists in the zirconium derivative.

PDF analysis of **Zr-PiPhtA** (Fig. 4a) shows that this solid does not exhibit atomic order beyond 30 Å, which is indicative of a nanocrystalline material. Upon comparing the PDF pattern of this compound with those of **Zr-BTTMP** and **Ca-PiPhtA** (Fig. 4b) in the short range region ($r < 5$ Å), a close similarity between **Zr-PiPhtA** and **Zr-BTTMP** suggests the presence of octahedral Zr^{4+} sites in the former rather than having a

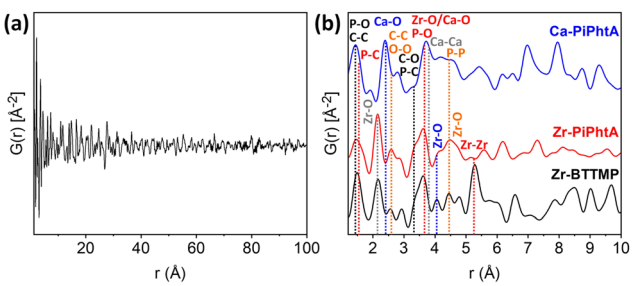

Fig. 4 (a) Experimental PDF pattern of **Zr-PiPhtA** and (b) comparison with the simulated ones of **Ca-PiPhtA** and **Zr-BTTMP** in the short-range order displaying selected bonding and non-bonding interatomic distances.

hepta-coordinated metal environment, as it is the case of **Ca-PiPhtA**.[24]

Morphologically, the **Zr-PiPhtA**, **Zr-PNA** and **Zr-BTTMP** samples are very different according to SEM images (Fig. S7). Accordingly, **Zr-PiPhtA** and **Zr-BTTMP** are composed of ladder-like and sheet-like submicrometric particles, respectively, while **Zr-PNA** is formed by elongated rectangular micrometric particles.

Adsorption of NH_3 and pyridine

As previously reported,[24,25,50] NH_3 adsorption may considerably improve proton conductivity properties. As a result, two new derivatives were obtained, **Zr-PiPhtA_NH$_3$** and **Zr-PNA_NH$_3$**, with NH_3/H_2O molar ratios of 6.5/6 and 3/4.5, respectively. Their corresponding powder diffraction patterns, which could not be indexed, reveal structural changes upon ammonia adsorption, compatible with a structural expansion resulting from $NH_3 + H_2O$ intercalation,[24] as suggested by the appearance of new diffraction peaks at low 2θ values (Fig. S8 and S9). Such changes are also accompanied by a partial amorphization. However, **Zr-BTTMP** did not experience any observable change after ammonia exposure (Fig. S10) and only a residual amount of ammonia was detected by elemental analysis (N, 0.134%), which may be due to the rigidity of the 3D framework where strong H-bond interactions occur and no space is available for small polar molecules, such as NH_3 and/or H_2O. The FTIR spectra of **Zr-PiPhtA_NH$_3$** (Fig. S11) and **Zr-PNA_NH$_3$** (Fig. S12) show a shift of the vibration bands towards lower wavenumbers in the stretching region (3460–3166 cm^{-1}), which may indicate the formation of strong H-bonds between guest molecules.[26] In addition, the new peaks appearing at 1400 and 1372 cm^{-1} in **Zr-PiPhtA_NH$_3$** and **Zr-PNA_NH$_3$**, respectively, can be assigned to the N–H deformation vibration of NH_4^+ ions.[51] On the other hand, the characteristic peak at around 1700 cm^{-1} corresponding to the carboxylic groups has practically disappeared, suggesting the interaction of these acidic groups with NH_3. The SEM images after ammonia vapour exposure of **Zr-PiPhtA_NH$_3$** and **Zr-PNA_NH$_3$** (Fig. S13) revealed the formation of micrometric agglomerates for both samples.

Pyridine adsorption was carried out to further characterize the acid sites on these solids. Fig. S14 shows the FT-IR spectra of the pyridine-loaded compounds. The FT-IR spectrum of **Zr-PiPhtA** shows bands at 1400 and 1450 cm^{-1} characteristic of Lewis acid sites. From elemental analysis, this material adsorbed 1.6 mmol g^{-1} of pyridine. In contrast, only traces of adsorbed pyridine were found for the two other solids. The pyridine treatment did not cause appreciable changes in the XRD patterns of the samples, suggesting that the internal acid sites are not accessible for this molecule.

Proton conductivity

The high-water content of **Zr-PiPhtA** and the presence of acidic phosphonate groups in both **Zr-PiPhtA** and **Zr-BTTMP** make these materials appropriate candidates for proton conduction. On the other hand, the anhydrous **Zr-PNA** derivative contains carboxylic groups as the unique acidic groups. The conductivity values as a function of the temperature at two RH values (95 and 75%) for the **Zr-PiPhtA**, **Zr-PNA** and **Zr-BTTMP** derivatives are plotted in Fig. 5 and the corresponding Nyquist plots at the different temperatures and humidities are shown in Fig. S15–S17. Possible chemical/structural changes of the samples after EIS measurements were monitored by LXRPD, TG and elemental (C, N, and H) analyses (Fig. S8–S10). All compounds exhibit water-mediated proton conductivity, as revealed by the increased values measured at higher RH. At 80 °C and 95% RH, the σ values followed the order: **Zr-BTTMP** (1.2×10^{-3} S cm^{-1}) > **Zr-PiPhtA** (5.5×10^{-4} S cm^{-1}) > **Zr-PNA** (1.1×10^{-4} S cm^{-1}). On NH_3 adsorption (Fig. 5), an increase in proton conductivity was observed for the resulting compounds **Zr-PiPhtA_NH$_3$** (3.2×10^{-3} S cm^{-1}) and **Zr-PNA_NH$_3$** (6.6×10^{-4} S cm^{-1}) at 80 °C and 95% RH.

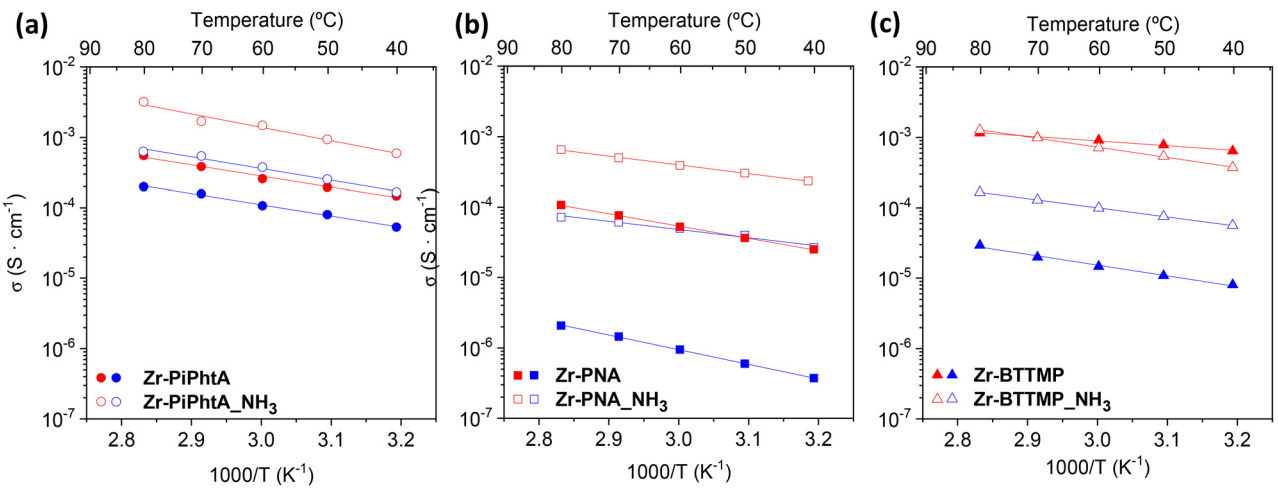

Fig. 5 Arrhenius plots at 95% RH (red) and 75% (blue) of Zr^{4+} phosphonates: (a) **Zr-PiPhtA**, (b) **Zr-PNA**, and (c) **Zr-BTTMP**.

With respect to the as-synthesized compound, the proton conductivity of **Zr-BTTMP_NH$_3$** remains almost invariable as measured at 95% RH, but it was enhanced at 75% RH (Fig. 5c). As elsewhere reported,[24] the adsorption of NH_3 also entails a concomitant adsorption of H_2O (Fig. S10). Thus, given the low loading of NH_3 in **Zr-BTTMP**, a significant increase in the proton conductivity would not be expected at high RH. However, the formation of strong H-bonds between the H_2O and NH_3 molecules could increase the retention of water at lower RHs, resulting in increased values of the proton conductivity. The enhancement in proton conductivity (one order of magnitude) observed for the ammonia-loaded compounds **Zr-PiPhtA_NH$_3$** and **Zr-PNA_NH$_3$** is attributed to cooperative ammonia and water adsorption, which allows for creating a more extended H-bond network between layers, in the case of **Zr-PiPhtA_NH$_3$**, or between chains, in the case of **Zr-PNA_NH$_3$**.

After two cycles of EIS measurements, the proton conductivity values for these compounds (Fig. S18) are comparable to those of other phosphonate-based proton conductors[52] such as **Ca-PiPhtA**,[24] (Me_2NH_2)[Eu(L)],[53] PCMOF-5 [54] and β-PCMOF-2,[55] and MOF-based materials, such as Co-MOF-74 [56] or UiO-66 (Zr)–$(CO_2H)_2$.[57] The activation energy values, ranging from 0.14 to 0.41 eV, are characteristics of a Grotthuss-type mechanism.[58,59]

Catalytic behaviour

Since zirconium phosphate/phosphonates derivatives are acidic catalysts active in FUR transformation, we have tested their performance for this reaction even though only the superficial acid sites are accessible to the pyridine molecule. The zirconium phosphonate derivatives, with BET surface areas <20 $m^2\ g^{-1}$, were tested in the one-pot reaction of furfural (Meerwein–Ponndorf–Verley reaction),[60,61] which is key to obtain valuable products, such as furfuryl alcohol (FOL), favoured by the presence of Lewis basic/acid sites, or iso-propyl furfuryl ether (iPFE), iso-propyl levulinate (iPL) or γ-valerolactone (GVL), promoted by Brønsted acid sites.[62]

As observed in Fig. 6a and Table S2, the most efficient catalyst for FUR removal at 24 h of reaction was **Zr-PiPhtA** (100%), followed by **Zr-BTTMP** (82%), while **Zr-PNA** showed a low efficiency (37%), a value even lower than that of the control catalyst $Zr_3(PO_4)_4$ (63%). Although FUR adsorption on the catalyst surface may also take place, the chemical reaction of FUR is expected to be the dominating factor at high temperatures (>393 K).[63] Both **Zr-PiPhtA** and **Zr-BTTMP** contain Lewis basic sites, *e.g.*, O^{2-} from Zr–O–P bonds,[34] and Brønsted acidic sites, *e.g.*, –COOH and/or $–PO_3H$. However, the accessibility to these sites is higher for the nanocrystalline **Zr-PiPhtA** than for the three-dimensional **Zr-BTTMP**, as revealed by NH_3 and pyridine

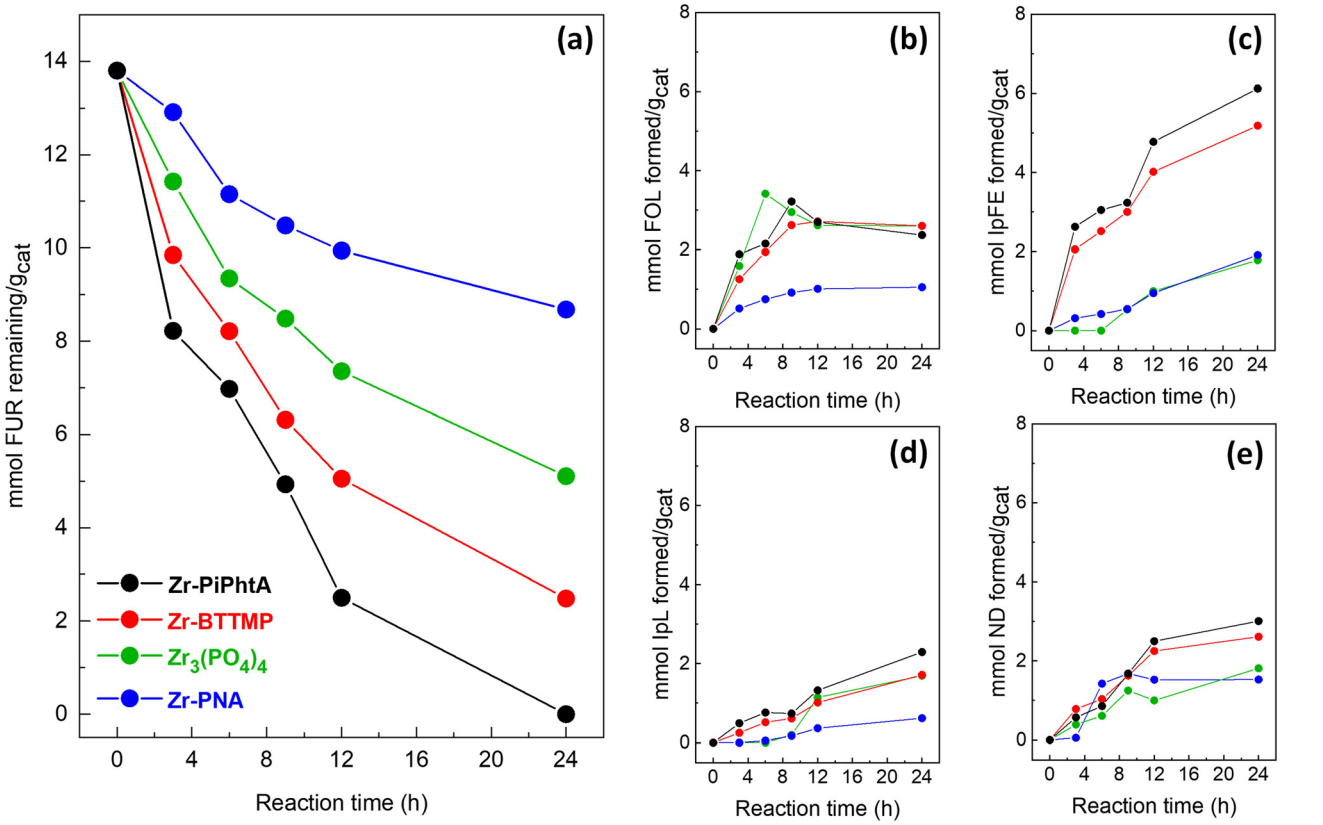

Fig. 6 Comparison of the catalytic behaviour of Zr^{4+} phosphonate and the corresponding phosphate in the FUR transformation: (a) remaining furfural and yields of (b) furfuryl alcohol, (c) iso-propyl furfuryl ether, (d) iso-propyl levulinate and (e) unidentified products. Reaction conditions: FUR: 0.1 mmol, catalyst: 0.025 g, 2-propanol: 4 mL, and 170 °C.

adsorption studies, which explain better FUR conversion for the former catalyst. The low activity observed for **Zr-PNA** can be rationalized by the limited accessibility of the FUR molecule to the active sites in this catalyst, which exhibits non-extended strong H-bond interactions between the $-NH^+$ groups and the F^- ions and between the $-PO_3^{2-}$ and carboxylic moieties.

FOL is mainly obtained at shorter reaction times by catalytic transfer of a hydride ion from the sacrificial alcohol (2-propanol) to the furfural through Lewis acid sites *via* a six-membered intermediate.[64] Yields of FOL, between 19 and 23%, were obtained after 9 h of reaction for the **Zr-PiPhtA** and **Zr-BTTMP** catalysts, which are comparable to that of $Zr_3(PO_4)_4$ (Fig. 6b and Table S1), from which the production of FOL reached a steady concentration. In contrast, the formation of iPFE, a valuable compound as a fuel additive,[65] continued increasing at high reaction times, a process requiring the accessibility of both Lewis and Brønsted acid sites,[62] which seems to be lower for the **Zr-PNA** and $Zr_3(PO_4)_4$ catalysts (Fig. 6c). A similar catalytic behaviour was observed to produce IP, which is obtained by ring-opening of iPFE catalysed by the Brønsted acid sites.[64,66] Once again, the most active catalysts for the latter reaction were **Zr-PiPhtA** and **Zr-BTTMP**, attributed to the remaining Brønsted acidic groups on the catalyst surface, accessible to this adsorbate (Fig. 6d). Finally, non-detected (ND) products (Fig. 6e) were also formed mainly after longer reaction times. Their formation was ascribed to undesired polymerization reactions, arising from the high reactivity of furfural and furfuryl alcohol.

Conclusions

Three new Zr(IV) phosphonates exhibiting catalytic and proton conductivity dual properties were successfully synthesized from phosphonic acids 5-(dihydroxyphosphoryl)-isophthalic acid (**PiPhtA**), 5-(dihydroxyphosphoryl)-nicotinic acid (**PNA**) and benzene-1,2,3-triyltris(methylenephosphonic acid) (**BTTMPA**). The 3D **Zr-BTTMP** and 1D **Zr-PNA** crystal structures have been solved from powder diffraction data, while for nanocrystalline **Zr-PiPhtA**, some structural details could be determined by PDF analysis, which revealed a lack of atomic order beyond 30 Å. This material, in comparison with **Zr-BTTMP** and the analogous **Ca-PiPhtA**, was inferred to display an octahedral coordination environment and structural resemblance with the calcium analogue.

All three compounds exhibited water-mediated proton conductivity, with values up to 1.2×10^{-3} S cm^{-1} at 80 °C and 95% RH for **Zr-BTTMP**. Upon exposure to ammonia vapours, **Zr-PNA** and **Zr-PiPhtA** exhibit a significant enhancement in proton conductivity, up to 3.2×10^{-3} S cm^{-1}, attributed to the formation of extended H-bond networks after the joint incorporation of water and ammonia. In addition, as compared to the control catalyst $Zr_3(PO_4)_4$, **Zr-PiPhtA** and **Zr-BTTMP** have shown remarkable activity in the one-pot transformation of furfural into valuable products such as furfuryl alcohol, isopropyl furfuryl ether, and iso-propyl levulinate. The superior performance of **Zr-PiPhtA** is attributed to the enhanced substrate accessibility derived from the nanocrystalline nature of this catalyst. Studies to enhance the accessibility to the catalytically active sites from the internal surface are underway.

Author contributions

The manuscript was written through the contributions of all authors. M. B.-G.: writing – original draft, synthesis and electrochemical measurements; R. M. P. C., P. O.-P. and A. C.: supervision, project administration, funding acquisition, and writing – review and editing; A. V.-C.: electrochemical measurements; J. A. C.: catalysis tests; and Ł. K. and J. Z.: synthesis of phosphonic acids and writing – review and editing. All authors have given approval to the final version of the manuscript.

Conflicts of interest

There are no conflicts to declare.

Data availability

The data supporting this study are available in Zenodo at https://doi.org/10.5281/zenodo.17628201.

The data supporting this article have been included as part of the supplementary information (SI). Supplementary information: Rietveld plots; XPS and FT-IR spectra and TG curves; X-ray thermodiffraction patterns; SEM images; XRPD patterns and TG curves; impedance plots. See DOI: https://doi.org/10.1039/d5dt02947c.

CCDC 2303569 and 2303570 contain the supplementary crystallographic data for this paper.[67a,b]

Acknowledgements

This work at UMA was funded by the Spanish and the European Union NextGenerationEU/PRTR research projects: PID2019-110249RB-I00/MCIN/AEI/10.13039/501100011033, PID2023-148883OB-I00/MCIU/AEI/10.13039/501100011033/FEDER, UE, TED2021-129836B-I00/MCIN/AEI/10.13039/501100011033, and PPRO-FQM113-G-2023 (Plan Propio UMA-Junta de Andalucia, Spain). Synchrotron X-ray powder diffraction studies were performed at the MSPD-04 beamline at ALBA Synchrotron Light with the collaboration of ALBA staff (experiment AV2022025742). M. B.-G. thanks B1-2023_006 (Plan Propio UMA) for financial support. A. V. C. thanks MICIU for the PRE2020-094459 student grant and the University of Malaga for financial support under the Plan Propio de Investigación. J. K. Z. acknowledges support from Academia Iuvenum, Wroclaw University of Science and Technology. Funding for open access charge: Universidad de Málaga/CBUA.

References

1 S. J. I. Shearan, N. Stock, F. Emmerling, J. Demel, P. A. Wright, K. D. Demadis, M. Vassaki, F. Costantino, R. Vivani, S. Sallard, I. R. Salcedo, A. Cabeza and M. Taddei, New Directions in Metal Phosphonate and Phosphinate Chemistry, *Crystals*, 2019, **9**, 270, DOI: 10.3390/cryst9050270.

2 C.-Y. Gao, J. Ai, H.-R. Tian, D. Wu and Z.-M. Sun, An ultra-stable zirconium-phosphonate framework as bifunctional catalyst for highly active CO_2 chemical transformation, *Chem. Commun.*, 2017, **53**, 1293–1296, DOI: 10.1039/C6CC08773F.

3 F. Costantino, M. Nocchetti, M. Bastianini, A. Lavacchi, M. Caporali and F. Liguori, Robust Zirconium Phosphate–Phosphonate Nanosheets Containing Palladium Nanoparticles as Efficient Catalyst for Alkynes and Nitroarenes Hydrogenation Reactions, *ACS Appl. Nano Mater.*, 2018, **1**(4), 1750–1757, DOI: 10.1021/acsanm.8b00193.

4 B. Shah and U. Chudasama, Kinetics, thermodynamics and metal separation studies of transition (Co^{2+}, Ni^{2+}, Cu^{2+}, Zn^{2+}) and heavy metal ions (Cd^{2+}, Hg^{2+}, Pb^{2+}) using novel hybrid ion exchanger—Zirconium amino tris methylene phosphonic acid, *Sep. Sci. Technol.*, 2019, **54**, 1560–1572, DOI: 10.1080/01496395.2018.1519580.

5 M. W. Terban, C. Shi, R. Silbernagel, A. Clearfield and S. J. L. Billinge, Local Environment of Terbium(III) Ions in Layered Nanocrystalline Zirconium(IV) Phosphonate-Phosphate Ion Exchange Materials, *Inorg. Chem.*, 2017, **56**, 8837–8846, DOI: 10.1021/acs.inorgchem.7b00666.

6 R. Silbernagel, C. H. Martin and A. Clearfield, Zirconium (IV) Phosphonate-Phosphates as Efficient Ion-Exchange Materials, *Inorg. Chem.*, 2016, **55**, 1651–1656, DOI: 10.1021/acs.inorgchem.5b02555.

7 R. Silbernagel, T. C. Shehee, C. H. Martin, D. T. Hobbs and A. Clearfield, Zr/Sn(IV) Phosphonates as Radiolytically Stable Ion-Exchange Materials, *Chem. Mater.*, 2016, **28**, 2254–2259, DOI: 10.1021/acs.inorgchem.5b02555.

8 J. Nakamura, R. Ito, R. Kozaki, A. Sugawara-Narutaki and C. Ohtsuk, Organic modification of layered zirconium phosphate/phosphonate for controlled release of therapeutic inorganic ions, *Sci. Technol. Adv. Mater.*, 2021, **22**, 1000–1012, DOI: 10.1080/14686996.2021.1993728.

9 T. Zheng, Z. Yang, D. Gui, Z. Liu, X. Wang, X. Dai, S. Liu, L. Zhang, Y. Gao and L. Chen, Overcoming the Crystallization and Designability Issues in the Ultrastable Zirconium Phosphonate Framework System, *Nat. Commun.*, 2017, **8**, 15369, DOI: 10.1038/ncomms15369.

10 C. Davide, S. Ravaioli, R. Vivani, A. Donnadio, E. Vischini, A. Russo, L. Visai, C. R. Arciola, L. Montanaro and M. Nocchetti, Antibacterial Properties of a Novel Zirconium Phosphate-Glycinediphosphonate Loaded with Either Zinc or Silver, *Materials*, 2019, **12**(19), 3184, DOI: 10.3390/ma12193184.

11 M. Nocchetti, A. Donnadio, E. Vischini, T. Posati, C. Albonetti, D. Campoccia, C. R. Arciola, S. Ravaioli, V. Mariani, L. Montanaro and R. Vivani, Synthesis, Crystal Structure, and Antibacterial Properties of Silver-Functionalized Low-Dimensional Layered Zirconium Phosphonates, *Inorg. Chem.*, 2022, **61**, 2251–2264, DOI: 10.1021/acs.inorgchem.1c03565.

12 F. Costantino, A. Donnadio and M. Casciola, Survey on the Phase Transitions and Their Effect on the Ion-Exchange and on the Proton-Conduction Properties of a Flexible and Robust Zr Phosphonate Coordination Polymer, *Inorg. Chem.*, 2012, **51**(12), 6992–7000, DOI: 10.1021/ic3009656.

13 M. Taddei, A. Donnadio, F. Costantino, R. Vivani and M. Casciola, Synthesis, Crystal Structure, and Proton Conductivity of One-Dimensional, Two-Dimensional, and Three-Dimensional Zirconium Phosphonates Based on Glyphosate and Glyphosine, *Inorg. Chem.*, 2013, **52**, 12131–12139, DOI: 10.1021/ic4019597.

14 A. Donnadio, M. Nocchetti, F. Costantino, M. Taddei, M. Casciola, F. da Silva Lisboa and R. Vivani, A Layered Mixed Zirconium Phosphate/Phosphonate with Exposed Carboxylic and Phosphonic Groups: X-ray Powder Structure and Proton Conductivity Properties, *Inorg. Chem.*, 2014, **53**, 13220–13226, DOI: 10.1021/ic502473w.

15 J. Zhang, L. Chen, D. Gui, H. Zhang, D. Zhang, W. Liu, G. Huang, J. Diwu, Z. Chai and S. Wang, An ingenious one-dimensional zirconium phosphonate with efficient strontium exchange capability and moderate proton conductivity, *Dalton Trans.*, 2018, **47**, 5161–5165, DOI: 10.1039/C8DT00508G.

16 S. M. F. Vilela, P. Salcedo-Abraira, A. Gómez-Peña, P. Trens, A. Várez, F. Salles and P. Horcajada, Proton Conductive Zr-Phosphonate UPG-1—Aminoacid Insertion as Proton Carrier Stabilizer, *Molecules*, 2020, **25**, 3519, DOI: 10.3390/molecules25153519.

17 M.-F. Qin, C.-Y. Wang, S.-S. Bao and L.-M. Zheng, Photoresponsive proton conduction in Zr-based metal–organic frameworks using the photothermal effect, *Chem. Commun.*, 2022, **58**, 8372–8375, DOI: 10.1039/D2CC02470E.

18 T. Zheng, W. Tan and L.-M. Zheng, Porous Metal Phosphonate Frameworks: Construction and Physical Properties, *Acc. Chem. Res.*, 2024, **57**, 2973–2984, DOI: 10.1021/acs.accounts.4c00337.

19 D. W. Kang, M. Kang, H. Kim, J. H. Choe, D. W. Kim, J. R. Park, W. R. Lee, D. Moon and C. S. Hong, A Hydrogen-Bonded Organic Framework (HOF) with Type IV NH_3 Adsorption Behavior, *Angew. Chem., Int. Ed.*, 2019, **58**, 16152–16155, DOI: 10.1002/anie.201911087.

20 B. Wang, R.-B. Lin, Z. Zhang, S. Xiang and B. Chen, Hydrogen-Bonded Organic Frameworks as a Tunable Platform for Functional Materials, *J. Am. Chem. Soc.*, 2020, **142**, 14399–14416, DOI: 10.1021/jacs.0c06473.

21 R.-B. Lin, Y. He, P. Li, H. Wang, W. Zhou and B. Chen, Multifunctional Porous Hydrogen-Bonded Organic Framework Materials, *Chem. Soc. Rev.*, 2019, **48**, 1362–1389, DOI: 10.1039/C8CS00155C.

22 Y. Wang, J. Yin, D. Liu, C. Gao, Z. Kang, R. Wang, D. Sun and J. Jiang, Guest-tuned proton conductivity of a porphyri-

nylphosphonate-based hydrogen-bonded organic framework, *J. Mater. Chem. A*, 2021, **9**, 2683–2688, DOI: 10.1039/D0TA07207A.

23 Y.-S. Wei, X.-P. Hu, Z. Han, X.-Y. Dong, S.-Q. Zang and T. C. W. Mak, Unique Proton Dynamics in an Efficient MOF-Based Proton Conductor, *J. Am. Chem. Soc.*, 2017, **139**, 3505–3512, DOI: 10.1021/jacs.6b12847.

24 M. Bazaga-García, R. M. P. Colodrero, M. Papadaki, P. Garczarek, J. Zoń, P. Olivera-Pastor, E. R. Losilla, L. León-Reina, M. A. G. Aranda, D. Choquesillo-Lazarte, K. D. Demadis and A. Cabeza, Guest Molecule-Responsive Functional Calcium Phosphonate Frameworks for Tuned Proton Conductivity, *J. Am. Chem. Soc.*, 2014, **136**(15), 5731–5739, DOI: 10.1021/ja500356z.

25 R. I. Salcedo, M. Bazaga-García, R. M. P. Colodrero, A. Vílchez-Cózar, F. Cañamero-Cebrián, P. Olivera-Pastor, J. K. Zaręba and A. Cabeza, Structural Landscape and Proton Conduction of Lanthanide 5-(Dihydroxyphosphoryl) isophthalates, *Cryst. Growth Des.*, 2024, **24**(19), 7910–7918, DOI: 10.1021/acs.cgd.4c00786.

26 B.-B. Hao, N. Qiao, Y. Rong, C.-X. Zhang and Q.-L. Wang, Bifunctional Metal–Organic Framework Functionalized by Dimethylamine Cations: Proton Conduction and Iodine Vapor Adsorption, *Inorg. Chem.*, 2022, **61**, 9533–9540, DOI: 10.1021/acs.inorgchem.2c00597.

27 H. Wang, Y. Zhao, Z. Shao, W. Xu, Q. Wu, X. Ding and H. Hou, Proton Conduction of Nafion Hybrid Membranes Promoted by NH_3-Modified Zn-MOF with Host–Guest Collaborative Hydrogen Bonds for H_2/O_2 Fuel Cell Applications, *ACS Appl. Mater. Interfaces*, 2021, **13**, 7485–7497, DOI: 10.1021/acsami.0c21840.

28 X.-F. Jiang, Y.-J. Ma, J.-X. Hu and G.-M. Wang, Optimizing the Proton Conductivity of Fe-Diphosphonates by Increasing the Relative Number of Protons and Carrier Densities, *Inorg. Chem.*, 2020, **59**, 11834–11840, DOI: 10.1021/acs.inorgchem.0c01919.

29 R. Liu, L. Zhao, S. Yu, X. Liang, Z. Li and G. Li, Enhancing Proton Conductivity of a 3D Metal–Organic Framework by Attaching Guest NH_3 Molecules, *Inorg. Chem.*, 2018, **57**, 11560–11568, DOI: 10.1021/acs.inorgchem.8b01606.

30 X. Liang, B. Li, M. Wang, J. Wang, R. Liu and G. Li, Effective Approach to Promoting the Proton Conductivity of Metal–Organic Frameworks by Exposure to Aqua–Ammonia Vapor, *ACS Appl. Mater. Interfaces*, 2017, **9**, 25082–25086, DOI: 10.1021/acsami.7b07635.

31 A. Donnadio, M. Pica, M. Nocchetti and O. Piermatti, Zirconium Phosphates and Phosphonates: Applications in Catalysis, *Catalysts*, 2024, **14**, 733, DOI: 10.3390/catal14100733.

32 W. Adhami, A. Richel and C. Len, A review of recent advances in the production of furfural in batch system, *Mol. Catal.*, 2023, **545**, 113178, DOI: 10.1016/j.mcat.2023.113178.

33 A. K. Manal and J. H. Advani, R. Srivastava, Bifunctional Acid–Base Zirconium Phosphonate for Catalytic Transfer Hydrogenation of Levulinic Acid and Cascade Transformation of Furfural to Biofuel Molecules, *ChemCatChem*, 2022, **14**, e202200576, DOI: 10.1002/cctc.202200576.

34 J. Song, B. Zhou, H. Zhou, L. Wu, Q. Meng, Z. Liu and B. Han, Porous Zirconium–Phytic Acid Hybrid: A Highly Efficient Catalyst for Meerwein–Ponndorf–Verley Reductions, *Angew. Chem., Int. Ed.*, 2015, **54**, 9399–9403, DOI: 10.1002/anie.201504001.

35 S. Bauer and N. Stock, Synthesis and characterization of four new metal 5-phosphonoisophthalates discovered by high-throughput experimentation, *J. Solid State Chem.*, 2007, **180**, 3111–3120, DOI: 10.1016/j.jssc.2007.08.026.

36 R. Chen, Y. Chen, X. Zeng, J. Li and X. Luo, Transition metal phosphonates with pyridyl-based phosphonic acids: synthesis, characterization and luminescence properties, *J. Coord. Chem.*, 2017, **706**, 949–959, DOI: 10.1080/00958972.2017.1280158.

37 C. Wang, P. Feng, J. Li and X. Luo, Synthesis, crystal structures and luminescence properties of two metal carboxyphosphonates, *J. Solid State Chem.*, 2017, **249**, 136–140, DOI: 10.1016/j.jssc.2017.02.019.

38 J. Li, R. Chen, X. Zeng, C. Wang, Y. Chen and X. Luo, Amine-templated synthesis of two metal phosphonates based on 5-phosphononicotinic acid, *Inorg. Chim. Acta*, 2016, **444**, 181–185, DOI: 10.1016/j.ica.2016.02.003.

39 J. Zoń, V. Videnova-Adrabinska, J. Janczak, M. Wilk, A. Samoc, R. Gancarz and M. Samoc, Design, synthesis and noncentrosymmetric solid state organization of three novel pyridylphosphonic acids, *CrystEngComm*, 2011, **13**, 3474–3484, DOI: 10.1039/C1CE05140G.

40 L. Pinkert, Y.-H. Lai, C. Peukert, S.-K. Hotop, B. Karge, L. M. Schulze, J. Grunenberg and M. Brönstrup, Antibiotic Conjugates with an Artificial MECAM-Based Siderophore Are Potent Agents against Gram-positive and Gram-negative Bacterial Pathogens, *J. Med. Chem.*, 2021, **64**, 15440–15460, DOI: 10.1021/acs.jmedchem.1c01482.

41 B. Graham, L. Spiccia, A. M. Bond, M. T. W. Hearn and C. M. Kepert, Structural, spectroscopic and electrochemical studies of nickel(II) "sandwich" complexes with ligands featuring tethered 1,4,7-triazacyclononane macrocycles, *J. Chem. Soc., Dalton Trans.*, 2001, 2232–2238, DOI: 10.1039/B101766G.

42 A. Altomare, C. Cuocci, C. Giacovazzo, A. Moliterni, R. Rizzi, N. Corriero and A. Falcicchio, EXPO2013: A Kit of Tools for Phasing Crystal Structures From Powder Data, *J. Appl. Crystallogr.*, 2013, **46**, 1231–1235, DOI: 10.1107/S0021889813013113.

43 H. M. Rietveld, A Profile Refinement Method for Nuclear and Magnetic Structures, *J. Appl. Crystallogr.*, 1969, **2**, 65–71, DOI: 10.1107/S0021889869006558.

44 B. H. Toby and R. B. Von Dreele, GSAS-II: The genesis of a modern open-source all purpose crystallography software package, *J. Appl. Crystallogr.*, 2013, **46**, 544–549, DOI: 10.1107/S0021889813003531.

45 P. Juhás, T. Davis, C. L. Farrow and S. J. L. Billinge, PDFgetX3: A rapid and highly automatable program for processing powder diffraction data into total scattering

pair distribution functions, *J. Appl. Crystallogr.*, 2013, **46**, 560–566, DOI: 10.1107/S0021889813005190.

46 C. L. Farrow, P. Juhás, J. W. Liu, D. Bryndin, E. S. Božin, J. Bloch, T. Proffen and S. J. L. Billinge, PDFfit2 and PDFgui: computer programs for studying nanostructure in crystals, *J. Phys.: Condens. Matter*, 2007, **19**, 335219, DOI: 10.1088/0953-8984/19/33/335219.

47 J. Jiménez-Jiménez, P. Maireles-Torres, P. Olivera-Pastor, E. Rodríguez-Castellón, A. Jiménez-López, D. J. Jones and J. Rozière, Surfactant-Assisted Synthesis of a Mesoporous Form of Zirconium Phosphate with Acidic Properties, *Adv. Mater.*, 1998, **10**, 812–815, DOI: 10.1002/(SICI)1521-4095(199807)10:10<812::AID-ADMA812>3.0.CO;2-A.

48 D. Y. Osadchii, A. I. Olivos-Suarez, A. V. Bavykina and J. Gascon, Revisiting Nitrogen Species in Covalent Triazine Frameworks, *Langmuir*, 2017, **33**, 14278–14285, DOI: 10.1021/acs.langmuir.7b02929.

49 A. Boultif and D. Louër, Powder pattern indexing with the dichotomy method, *J. Appl. Crystallogr.*, 2004, **37**, 724–731, DOI: 10.1107/S0021889804014876.

50 I. R. Salcedo, M. Bazaga-García, A. Cuesta, E. R. Losilla, K. D. Demadis, P. Olivera-Pastor, R. M. P. Colodrero and A. Cabeza, NH_3/H_2O-mediated proton conductivity and photocatalytic behaviour of Fe(II)-hydroxyphosphonoacetate and M(II)-substituted derivatives, *Dalton Trans.*, 2020, **49**, 3981–3988, DOI: 10.1039/C9DT04210E.

51 A. Micek-Ilnicka, B. Gil and E. Lalik, Ammonia Sorption by Dawson Acid Studied by IR Spectroscopy and Microbalance, *J. Mol. Struct.*, 2005, **740**, 25–29, DOI: 10.1016/j.molstruc.2005.01.001.

52 S.-S. Bao, G. K. H. Shimizu and L.-M. Zheng, Proton Conductive Metal Phosphonate Frameworks, *Coord. Chem. Rev.*, 2019, **378**, 577–594, DOI: 10.1016/j.ccr.2017.11.029.

53 Y.-S. Wei, X.-P. Hu, Z. Han, X.-Y. Dong, S.-Q. Zang and T. C. W. Mak, Unique Proton Dynamics in an Efficient MOF-Based Proton Conductor, *J. Am. Chem. Soc.*, 2017, **139**, 3505–3512, DOI: 10.1021/jacs.6b12847.

54 J. M. Taylor, K. W. Dawson and G. K. H. Shimizu, A Water-Stable Metal–Organic Framework with Highly Acidic Pores for Proton-Conducting Applications, *J. Am. Chem. Soc.*, 2013, **135**, 1193–1196, DOI: 10.1021/ja310435e.

55 J. Hurd, R. Vaidhyanathan, V. Thangadurai, C. I. Ratcliffe, I. L. Moudrakovski and S. H. Shimizu, Anhydrous proton conduction at 150 °C in a crystalline metal–organic framework, *Nat. Chem.*, 2009, **1**, 705–710, DOI: 10.1038/nchem.402.

56 S. Hwang, E. J. Lee, D. Song and N. C. Jeong, High Proton Mobility with High Directionality in Isolated Channels of MOF-74, *ACS Appl. Mater. Interfaces*, 2018, **10**, 35354–35360, DOI: 10.1021/acsami.8b11816.

57 D. D. Borges, S. D. Vinot, H. Jobic, J. Ollivier, F. Nouar, R. Semino, T. Devic, C. Serre, F. Paesani and G. Maurin, Proton Transport in a Highly Conductive Porous Zirconium-Based Metal-Organic Framework: Molecular Insight, *Angew. Chem., Int. Ed.*, 2016, **55**, 3919–3924, DOI: 10.1002/anie.201510855.

58 N. Agmon, The Grotthuss Mechanism, *Chem. Phys. Lett.*, 1995, **244**(56), 456–462, DOI: 10.1016/0009-2614(95)00905-J.

59 P. Colomban, in *Proton Conductors: Solids, Membranes and Gels Materials and Devices, Chemistry of Solid State Materials*, Cambridge University Press, Cambridge, U.K., 1992, vol. 2.

60 T. Komanoya, K. Nakajima, M. Kitano and M. Hara, Synergistic catalysis by Lewis acid and base sites on ZrO_2 for Meerwein–Ponndorf–Verley reduction, *J. Phys. Chem. C*, 2015, **119**, 26540–26546, DOI: 10.1021/acs.jpcc.5b08355.

61 F. Gonell, M. Boronat and A. Corma, Structure–reactivity relationship in isolated Zr sites present in Zr-zeolite and ZrO_2 for the Meerwein–Ponndorf–Verley reaction, *Catal. Sci. Technol.*, 2017, **7**, 2865–2873, DOI: 10.1039/C7CY00567A.

62 M. J. Gilkey and B. Xu, Heterogeneous catalytic transfer hydrogenation as an effective pathway in biomass upgrading, *ACS Catal.*, 2016, **6**, 1420–1436, DOI: 10.1021/acscatal.5b02171.

63 A. Kumar and R. Srivastava, Zirconium Phosphate Catalyzed Transformations of Biomass-Derived Furfural to Renewable Chemicals, *ACS Sustainable Chem. Eng.*, 2020, **8**, 9497–9506, DOI: 10.1021/acssuschemeng.0c02439.

64 L. Bui, H. Luo, W. R. Gunther and Y. Román-Leshkov, Domino reaction catalyzed by zeolites with Brønsted and Lewis acid sites for the production of γ-valerolactone from furfural, *Angew. Chem.*, 2013, **125**, 8180–8183, DOI: 10.1002/ange.201302575.

65 T. A. Natsir and S. Shimazu, Fuels and fuel additives from furfural derivatives via etherification and formation of methylfurans, *Fuel Process. Technol.*, 2020, **200**, 106308, DOI: 10.1016/j.fuproc.2019.106308.

66 A. Démolis, N. Essayem and F. Rataboul, Synthesis and applications of alkyl levulinates, *ACS Sustainable Chem. Eng.*, 2014, **2**, 1338–1352, DOI: 10.1021/sc500082n.

67 (*a*) CCDC 2303569: Experimental Crystal Structure Determination, 2026, DOI: 10.5517/ccdc.csd.cc2hb1pl; (*b*) CCDC 2303570: Experimental Crystal Structure Determination, 2026, DOI: 10.5517/ccdc.csd.cc2hb1qm.